Multi-messenger NS mergers: using GWs and photon light-curves to understand their properties

M. Ángeles Pérez-García

Department of Fundamental Physics,
University of Salamanca, SPAIN; mperezga@usal.es

& Albertus C 1, Barba D 1, Bulla M 3, Pérez E 4, Sagués-Carracedo A 3, Izzo L 2 , Dhawan S 5 , Prada F 4

1 Department of Fundamental Physics and IUFFyM, Universidad de Salamanca, Salamanca, Spain; 2 DARK, Niels Bohr Institute, University of Copenhagen, Copenhagen, Denmark; 3 The Oskar Klein Centre, Department of Astronomy, Stockholm University, Stockholm, Sweden; 4 Instituto de Astrofísica de Andalucía (CSIC), Granada, Spain; 5 Kavli Institute for Cosmology, Institute of Astronomy, Cambridge, United Kingdom

Outline

- Binary Neutron Stars: Multimessenger events.
- Input from NS physics: EoS
- EM Waves+GW: Kilonova properties and Modeling
- Conclusions

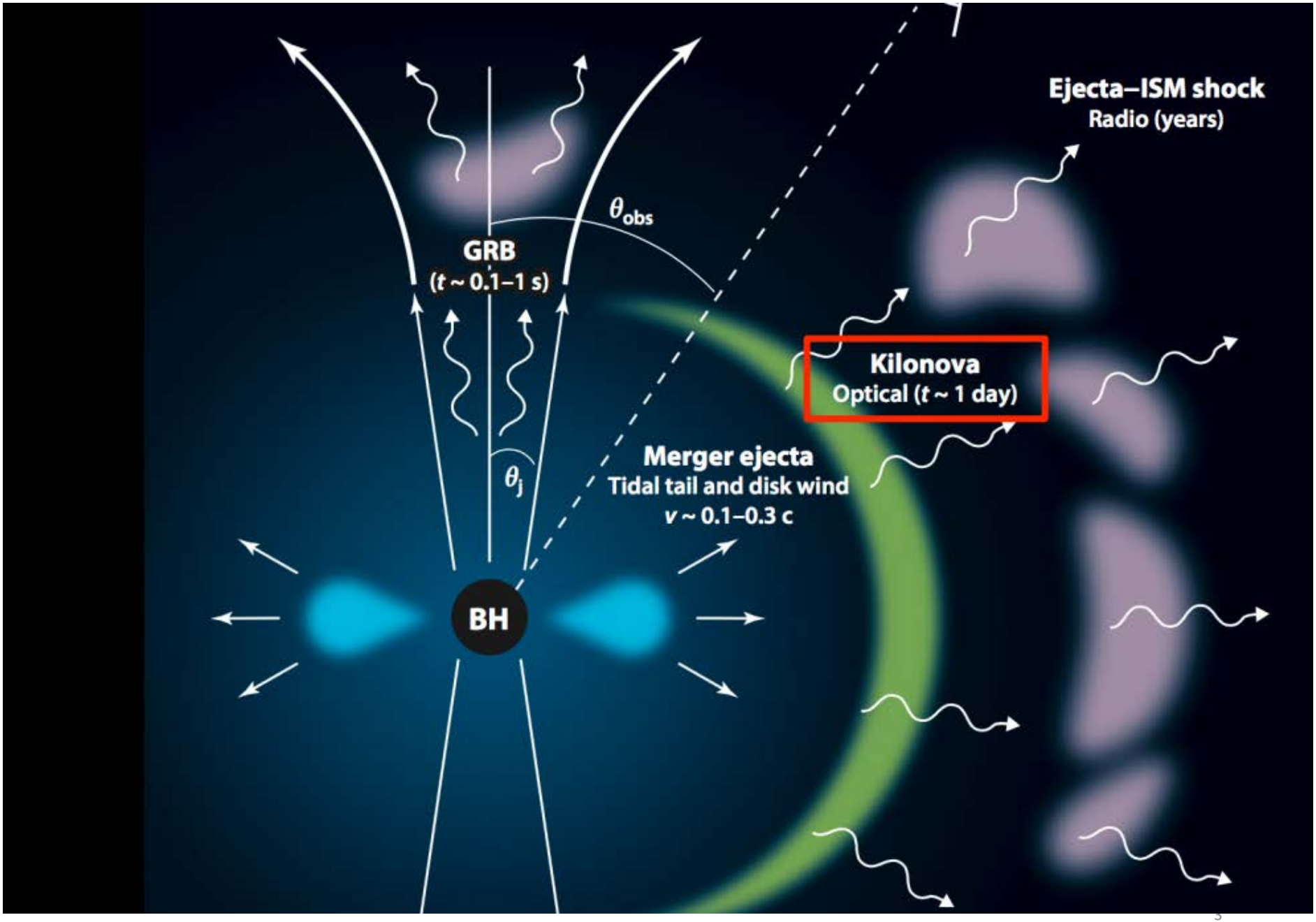

courtesy of B. Metzger

BNS: Multimessenger events

•Theoretically we expect multimessengers: GW+EM+neutrinos+X

•One previous event associated to GW170817: EM band
•Other KN (involving NS): no EM counterpart e.g. 190814, GW200105, GW200115 and many other.

GW170817+AT2017gfo+GRB2017A

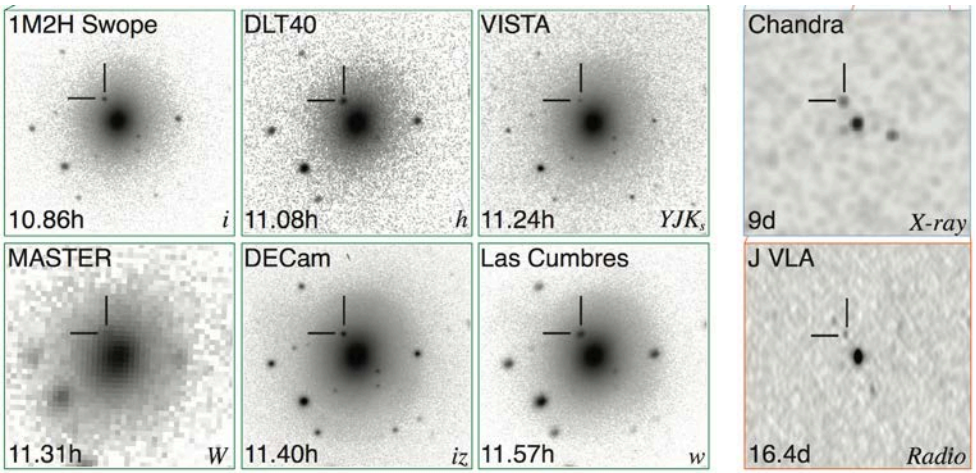

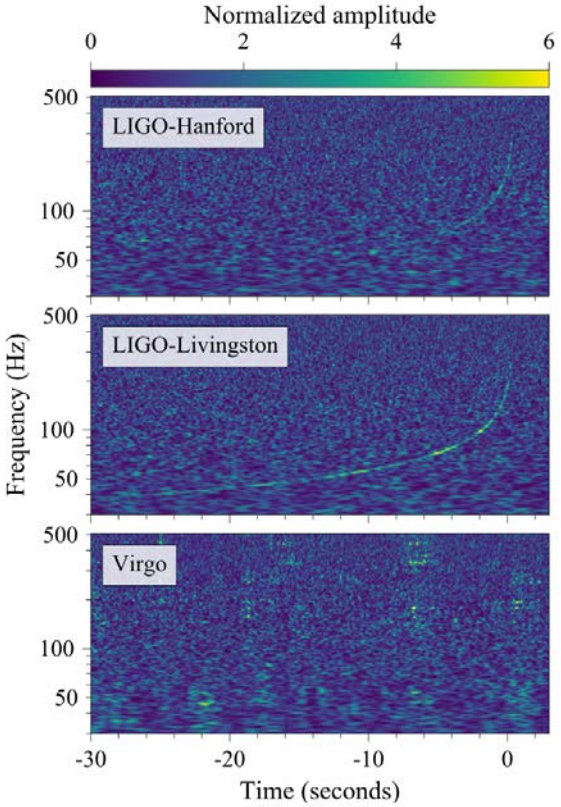

Historical event: GW170817

TABLE II. Properties for GW170817 inferred using the PhenomPNRT waveform model. All properties are source properties except for the detector-frame chirp mass $\mathcal{M}^{\rm det} = \mathcal{M}(1+z)$. Errors quoted as x^{+z}_{-y} represent the median, 5% lower limit, and 95% upper limit. Errors quoted as (x, y) are one-sided 90% lower or upper limits, and they are used when one side is bounded by a prior. For the masses, m_1 is bounded from below and m_2 is bounded from above by the equal-mass line. The mass ratio is bounded by $q \leq 1$. For the tidal parameter $\tilde{\Lambda}$, we quote results using a constant (flat) prior in $\tilde{\Lambda}$. In the high-spin case, we quote a 90% upper limit for $\tilde{\Lambda}$, while in the low-spin case, we report both the symmetric 90% credible interval and the 90% highest posterior density (HPD) interval, which is the smallest interval that contains 90% of the probability.

	Low-spin prior ($\chi \leq 0.05$)	High-spin prior ($\chi \leq 0.89$)
Binary inclination θ_{JN}	146^{+25}_{-27} deg	152^{+21}_{-27} deg
Binary inclination θ_{JN} using EM distance constraint [108]	151^{+15}_{-11} deg	153^{+15}_{-11} deg
Detector-frame chirp mass $\mathcal{M}^{\rm det}$	$1.1975^{+0.0001}_{-0.0001}$ $M_\odot$	$1.1976^{+0.0004}_{-0.0002}$ $M_\odot$
Chirp mass $\mathcal{M}$	$1.186^{+0.001}_{-0.001}$ $M_\odot$	$1.186^{+0.001}_{-0.001}$ $M_\odot$
Primary mass m_1	$(1.36, 1.60)$ $M_\odot$	$(1.36, 1.89)$ $M_\odot$
Secondary mass m_2	$(1.16, 1.36)$ $M_\odot$	$(1.00, 1.36)$ $M_\odot$
Total mass m	$2.73^{+0.04}_{-0.01}$ $M_\odot$	$2.77^{+0.22}_{-0.05}$ $M_\odot$
Mass ratio q	$(0.73, 1.00)$	$(0.53, 1.00)$
Effective spin $\chi_{\rm eff}$	$0.00^{+0.02}_{-0.01}$	$0.02^{+0.08}_{-0.02}$
Primary dimensionless spin χ_1	$(0.00, 0.04)$	$(0.00, 0.50)$
Secondary dimensionless spin χ_2	$(0.00, 0.04)$	$(0.00, 0.61)$
Tidal deformability $\tilde{\Lambda}$ with flat prior	300^{+500}_{-190}(symmetric)/300^{+420}_{-230}(HPD)	$(0, 630)$

Impact of EoS on simulated spectra

- We use:
- a) a set of nuclear EoS:DD2, SFHo, LS220 and NR simulations Radice et al 2018 and Nedora et al 2021
- b) spectra generated with POSSIS (Bulla 2019)

Pérez-García et al, arXiv:2204.00022 [astro-ph.CO]

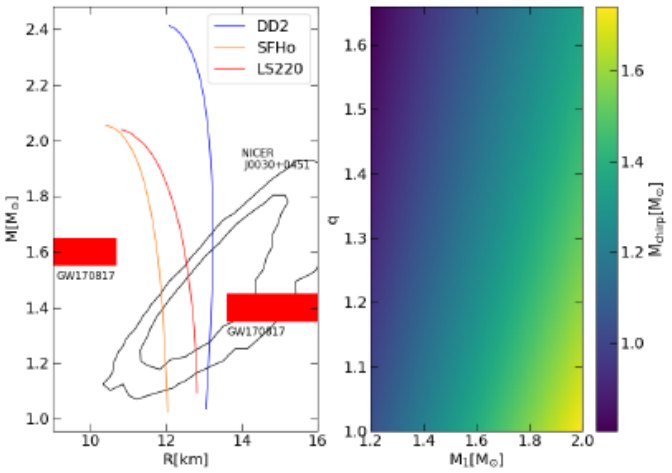

Fig. 6. (Left panel) Mass-radius relation for the three EoS that we use in this work DD2 (Typel et al. 2010), SFHo (Steiner et al. 2013) and LS220 (Lattimer & Swesty 1991). We also include radii constraints from GW170817 (Bauswein et al. 2017; Annala et al. 2018) and NICER (Miller et al. 2019). (Right panel) Values of chirp mass as a function of mass ratio q and the largest of the NS masses, M_1.

$$M_{\rm chirp} = \mathcal{M} = \left[\frac{q}{(1+q)^2}\right]^{3/5} M$$

Run	EoS	q	$M_{\rm chirp}\ (M_\odot)$	$M_1\ (M_\odot)$	$M_{\rm wind}\ (M_\odot)$	$M_{\rm dyn}\ (M_\odot)$	$\langle v_\theta \rangle / c$	$\langle Y_e \rangle$
1	DD2	1	1.22	1.4	3.708×10^{-2}	4×10^{-4}	0.22	0.17
2	SFHo	1	1.22	1.4	3×10^{-5}	4×10^{-4}	0.35	0.19
3	DD2	1	1.39	1.6	5.88×10^{-3}	1.2×10^{-3}	0.24	0.14
4	DD2	1	1.31	1.5	5.31×10^{-2}	7.0×10^{-4}	0.17	0.2
5	DD2	1.036	1.23	1.44	4.32×10^{-2}	5.0×10^{-4}	0.2	0.17
6	SFHo	1.036	1.23	1.44	2.7×10^{-4}	4.0×10^{-4}	0.33	0.18
7	LS220	1	1.22	1.4	1.37×10^{-2}	1.4×10^{-3}	0.17	0.14
8	LS220	1.036	1.23	1.44	1.17×10^{-2}	1.9×10^{-3}	0.16	0.14
9	LS220	1	1.31	1.5	4.80×10^{-4}	3.0×10^{-4}	0.19	0.08
10	LS220	1	1.39	1.6	2.10×10^{-4}	3.0×10^{-4}	0.21	0.07
11	LS220	1	1.49	1.71	1.80×10^{-4}	3.0×10^{-4}	0.22	0.08
12	SFHo	1.092	1.137	1.365	2.64×10^{-2}	1.5×10^{-3}	0.23	0.14
13	SFHo	1.17	1.128	1.4	3.52×10^{-2}	1.2×10^{-3}	0.2	0.14
14	SFHo	1	1.175	1.35	1.87×10^{-2}	3.50×10^{-3}	0.24	0.17
A	LS220	1	1.188	1.365	2.16×10^{-2}	1.6×10^{-3}	0.16	0.22
B	DD2	1	1.188	1.365	4.62×10^{-2}	1.1×10^{-3}	0.18	0.25
C	SFHo	1	1.188	1.365	5.67×10^{-3}	2.8×10^{-3}	0.21	0.23
D	DD2	1.43	1.188	1.637	9.12×10^{-2}	7.0×10^{-3}	0.14	0.14
E	LS220	1.43	1.188	1.637	5.34×10^{-2}	7.3×10^{-3}	0.17	0.16
F	LS220	1.66	1.188	1.769	2.04×10^{-2}	1.11×10^{-2}	0.14	0.07
G	DD2	1.22	1.188	1.509	6.27×10^{-2}	2.50×10^{-3}	0.17	0.19
H	SFHo	1.43	1.188	1.637	6.03×10^{-2}	3.80×10^{-3}	0.2	0.14
I	SFHo	1.66	1.188	1.769	5.31×10^{-2}	1.50×10^{-3}	0.12	0.07

KN emission from radioactive decay of ejecta

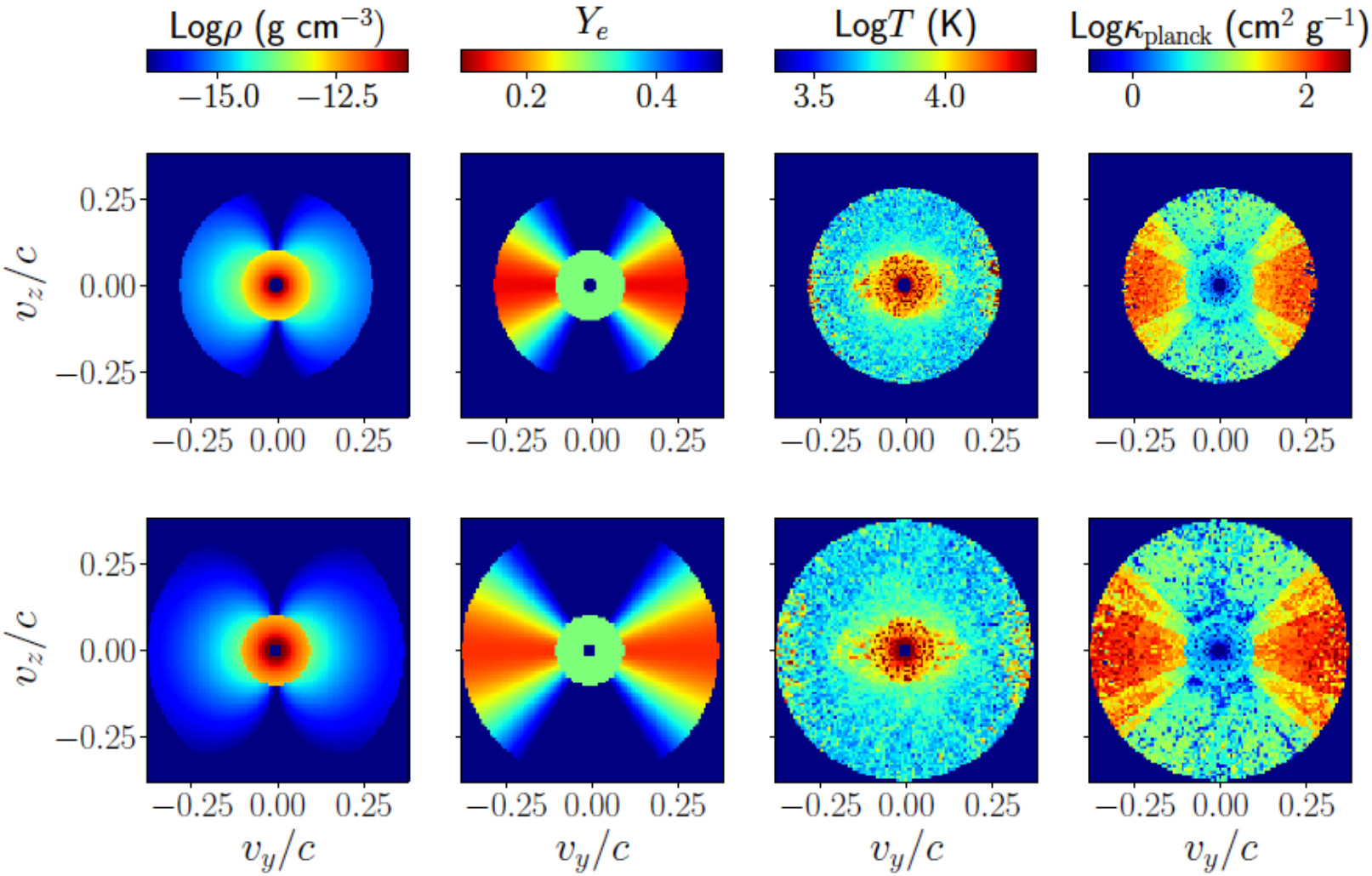

Fig. 5. From left to right, distributions of mass density ρ, electron fraction Y_e, temperature T and Planck mean opacities $\kappa_{\rm planck}$ in the $v_y - v_z$ velocity plane. The top row refers to run A (LS220 EoS) and the bottom row to run B (DD2 EoS), both with $q = 1$ and $M_{\rm chirp} = 1.188\,M_\odot$, see Table 1. Maps are computed at an epoch of 1 d after the merger. The pixelization seen in the T (and hence also $\kappa_{\rm planck}$) map is due to the temperature being computed with estimators in the code and thus being subject to Monte Carlo noise (see text for more details). Analytic functions are instead used for ρ and Y_e and the distributions are therefore smoother.

Orientation of KN: from polar to equatorial observer

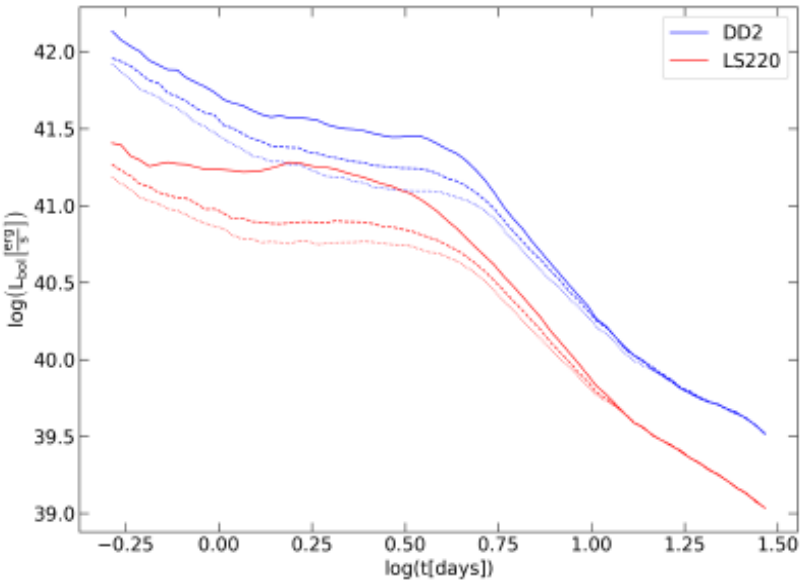

Fig. 3. Luminosity as a function of time obtained from two selected simulations concerning run 1 with EoS DD2 (blue line) and run 2 with EoS LS220 (red line), see Table 1. Solid, dashed and dotted lines refer to inclination angles $\cos\theta = 1, 0.7, 0$, respectively.

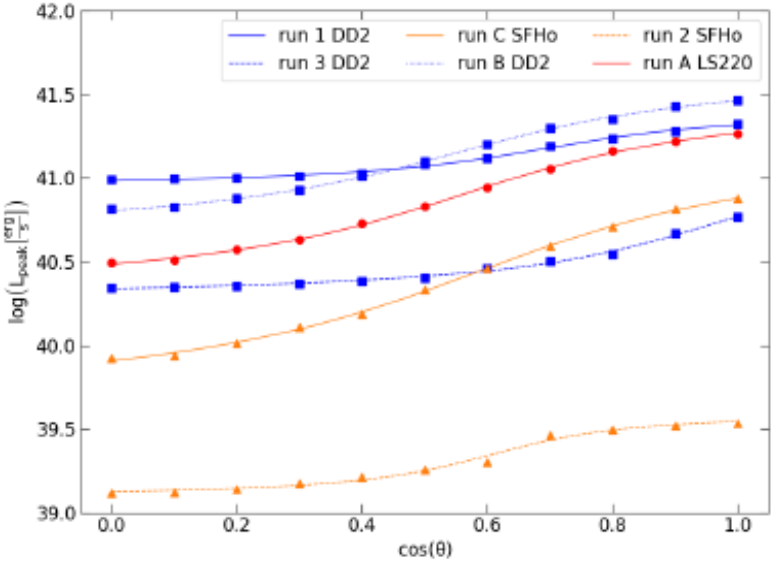

Fig. 15. Peak bolometric luminosity as a function of $\cos\theta$ and fitting functions. LS220, SFHo and DD2 EoS are shown in red, orange and blue colors, respectively. Runs A, B and C have a fixed $M_{\rm chirp} = 1.118 M_\odot$. Runs 1, 2 have $M_{\rm chirp} = 1.22 M_\odot$ and Run 3 has $M_{\rm chirp} = 1.39 M_\odot$. A fixed $q = 1$ value is used.

Pérez-García et al, arXiv:2204.00022 [astro-ph.CO]

$$\log L_{\rm peak}(x) = c_0 + c_1 \arctan(c_2(x - c_3))$$

$$x = \cos\theta.$$

Tidal polarizability and KN ejecta

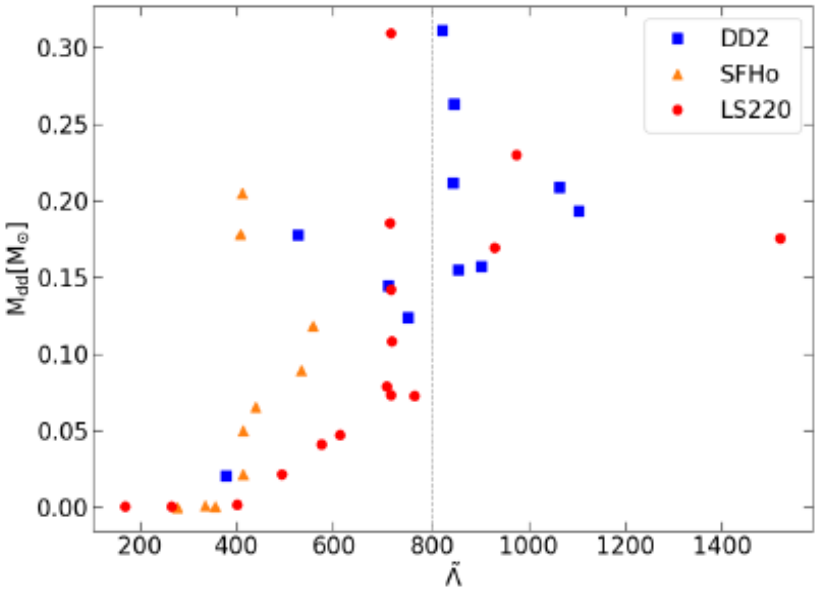

ig. 8. Dynamical plus disk mass, M_{dd}, as a function of $\tilde{\Lambda}$ for runs from Radice et al. 2018) and (Nedora et al. 2021), along with the $\tilde{\Lambda} = 800$ mit (Abbott et al. 2017) depicted as a vertical dashed line.

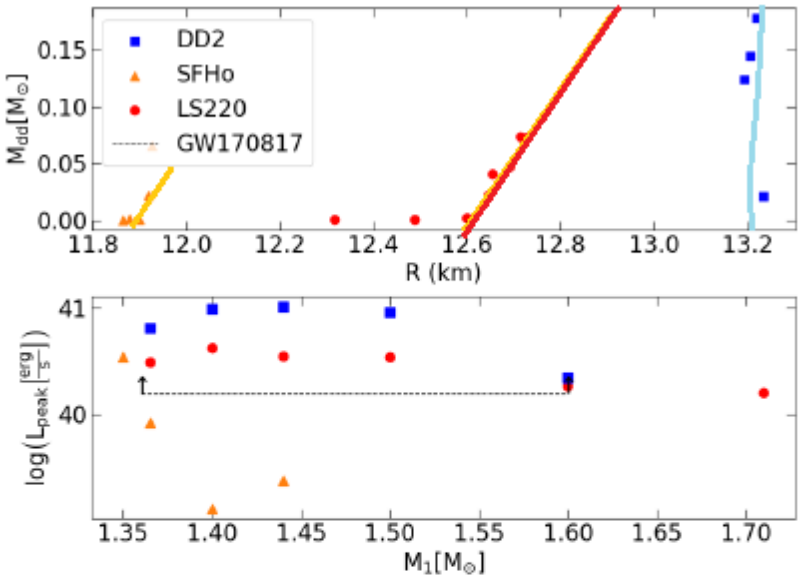

Fig. 10. (Top panel) M_{dd} as a function of NS radius from NR runs due to Radice et al. 2018 and Nedora et al. 2021 having $q \simeq 1$. (Bottom panel) $\log\left(L_{peak}[erg/s]\right)$ for an equatorial orientation as a function of primary mass M_1, for runs in Table 1 also having $q \simeq 1$.We also indicate a conservative lower limit estimate of equatorial peak luminosity for a GW170817-like transient.

Disk mass seems correlated to tidal polarizability.
GW170817 constrained it to less than about 720-800, Abbott et al 2017,2019.

$$\tilde{\Lambda} \equiv \frac{16}{13}\left[\frac{\Lambda_1 M_1^4 (M_1 + 12M_2) + \Lambda_2 M_2^4 (M_2 + 12M_1)}{(M_1 + M_2)^5}\right].$$

Pérez-García et al, arXiv:2204.00022 [astro-ph.CO]

Optical observations: MAAT @GTC

•Will display capabilities for observation IR-O-UV of next KN and possibly check complementary information regarding GW+EM.

Additional interest for H0 determination

•White paper: F Prada et al, arXiv:2007.01603 **[astro-ph.IM]**

Expected operation in mid 2024.

Sky	Telescope	Instrument	Spectral range	Resolution	Field of View	Spatial sampling	IFU
Southern	VLT	MUSE	480–930 nm	1770–3590	$59.9'' \times 60.0''$	$0.2'' \times 0.2''$	mirror slicer
Northern	Keck	KCWI	350–560 nm	3000–4000	$8.25'' \times 20.0''$	$0.34'' \times 0.147''$	mirror slicer
Northern	GTC	MAAT	360–1000 nm	600–4100	$12.0'' \times 8.5''$	$0.303'' \times 0.127''$	mirror slicer

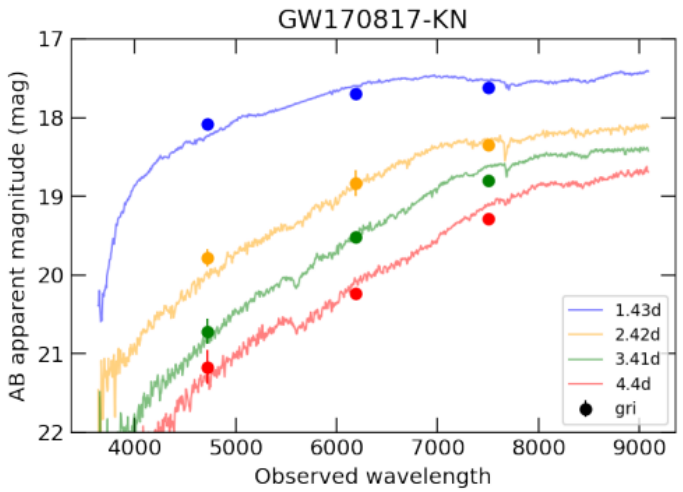

Fig. 18. Time series of X-shooter AT 2017gfo spectra as if observed with MAAT with the OSIRIS R1000B and R1000R grisms for 0.5 hr exposure per epoch. The observed broad-band SDSS *gri* magnitudes are also shown with circular markers (Smartt et al. 2017; Pian et al. 2017). Note that AT 2017gfo was found in a nearby galaxy at 40 Mpc and with an almost polar inclination angle direction ~20° (Hotokezaka et al. 2019).

Conclusions

- Binary Neutron Star detection in GW+EM will bring additional constraints on the nuclear EoS.

- We have simulated spectra and synthetic light curves with state of the art code POSSIS using Monte Carlo radiative transport with input from NR codes using a set of 3 EoS.

- Dynamical and disk masses being stripped off the binary are responsible for luminosity curves .

- Orientation effects may bias the peak quantities if not properly accounted for.

- Compactness for q~1 events shows correlation to peak luminosities and signals limit radius for the NS provided individual mass is known.

Thank you.